Electronic Supporting Information

In situ synthesis of Ni/NiO composites with defect ultrathin nanosheets for highly efficient biomass-derivatives selective hydrogenation

Yunan Wang[1], Feng Cao[*1], Weiwei Lin[*2, 3], Fengyu Zhao[2, 3], Jun Zhou[1], Song Li[*1], Gaowu Qin[1, 4]

[1]*Key Laboratory for Anisotropy and Texture of Materials (Ministry of Education), School of Material Science and Engineering, Northeastern University, Shenyang 110819, China*

[2]*State Key Laboratory of Electroanalytical Chemistry, Changchun Institute of Applied Chemistry, Chinese Academy of Sciences, Changchun 130022, P. R. China*

[3]*Jilin Province Key Laboratory of Green Chemistry and Process, Changchun Institute of Applied Chemistry, Chinese Academy of Sciences, Changchun 130022, P. R. China*

[*]*caof@atm.neu.edu.cn*
[*]*linwei@ciac.ac.cn*
[*]*lis@atm.neu.edu.cn*

Experimental section

Preparation of catalysts

All chemicals were of analytical grade and used as received. $Ni(OH)_2$ precursor was firstly prepared through the same method as our previous reports.[1] In a typical synthesis, 2 mmol of $Ni(NO_3)_2 \bullet 6H_2O$ was dissolved in 40 ml of distilled water to form a homogeneous solution by constant strong stirring. Then, 6 mmol of $NaBH_4$ was added to the above solution at room temperature and continually stirred for 5 min. The resulting reaction mixture was transferred into a Teflon-lined stainless autoclave (50 ml capacity). The autoclave was sealed and maintained in an electric oven at 180 ^oC for 2 h, and then cooled to room temperature naturally. The product was carefully collected and washed with distilled water and absolute ethanol several times, and then dried in a vacuum at 60 ^oC for 12 h. Then, $Ni(OH)_2$ samples were further to be calcined at 500 ^oC for 2 h in the air to prepare NiO. Finally, NiO samples were reduced at the atmosphere of hydrogen at 400, 450, 500 and 550 ^oC for 1 h, respectively. They were labelled as Ni/NiO-400, Ni/NiO-450, Ni/NiO-500 and

Ni/NiO-550 (400, 450, 500 and 550 refer to the reduction temperature). Ni/NiO composite catalysts with different metal contents were then obtained.

To further verify the unique advantages of the defected ultrathin supports, another Ni/NiO composite catalysts with relatively thick supports were prepared with a similar method. Pure flower-like $Ni(OH)_2$ precursor was firstly synthesized through a simple hydrothermal method, according to the previous report.[2] In a typical synthesis, 5 mmol of $Ni(NO_3)_2 \bullet 6H_2O$, 0.01 mmol of NH_4F and 0.03 mmol urea were dissolved in 40 ml of distilled water to form a homogeneous solution by constant strong stirring. The resulting reaction mixture was transferred into a Teflon-lined stainless autoclave (50 ml capacity). The autoclave was sealed and maintained in an electric oven at 120 ^oC for 6 h, and then cooled to room temperature naturally. The product was carefully collected and washed with distilled water and absolute ethanol several times, and then dried in a vacuum at 60 ^oC for 12 h. Then, the precursor was also calcined at 500 ^oC and subsequently reduced at 250, 300 and 400 ^oC for an hour at the atmosphere of hydrogen, respectively. And the obtained samples are labelled NiO-thick nanosheets, Ni/NiO-250- thick nanosheets, Ni/NiO-300-thick nanosheets and Ni/NiO-400-thick nanosheets, respectively.

Characterization of catalysts

The X-ray diffraction patterns (XRD) were obtained with a Rigaku-D/max 2500 V X-ray diffractometer with Cu Kα radiation (λ = 1.5418 Å). The morphologies and microstructures of catalysts were observed by field emission scanning electron microscopy (FE-SEM, JEOL JEM-2100F at 30 kV) and transmission scanning electron microscopy (TEM, JEOL JEM-200CT at 200 kV). High-resolution transmission scanning electron microscopy (HRTEM) image was obtained using the same experimental condition with TEM analysis. The X-ray photoelectron spectroscopy (XPS) analysis was performed on Thermo ESCALAB 250 electron spectrometer using Al Kα X-ray. The binding energies of XPS spectral range were calibrated for specimen charging effects using the C 1s level at the energy of 284.8 eV as a reference. To exclude the effects of air on the surface of samples, Ar^+ sputtering has been carried out before the test with the speed of 0.1 nm/s. N_2 adsorption–

desorption isotherms were measured by a Tristar II instrument. Specific surface areas were calculated using the Brunauer–Emmett–Teller (BET) model, and pore size distributions were evaluated from the desorption branches of the nitrogen isotherms using the Barrett–Joyner–Halenda (BJH) model. The water vapor adsorption kinetic curves and isotherms of the samples were measured at 25 ^{o}C by using a HydroWin (Quantachrome Instruments). Temperature programmed reduction (TPR), temperature programmed desorption (TPD) and temperature programmed oxidation (TPO) tests were measured on Micromeritics AutoChem II 2920 equipped with a thermal conduction detector (TCD) detector. For H_2-TPR analysis, 50 mg of the catalyst sample was placed in a quartz reactor and reduced by a 5% H_2-He gas mixture in a flow rate of 60 ml/min with temperature ramping at 10 ^{o}C/min until 800 ^{o}C. And the hydrogen consumption was determined using a TCD. For H_2-TPD experiments, 50 mg of the catalyst sample was pre-reduced for 2 h in a flow of He at 300 ^{o}C, and then cooled down to 40 ^{o}C. Next, the catalyst was exposed to a 5% H_2-He gas mixture in a flow rate of 60 ml/min for 3 h followed by sweeping with He at a flow rate of 20 ml/min for 1 h. Meanwhile, the temperature was linearly increased to 800 ^{o}C at a ramp rate of 10 ^{o}C/min to make hydrogen desorbed, and the TPD spectra were recorded. For TPO analysis, 50 mg of the catalyst sample was placed in a quartz reactor and reduced by a 5% O_2-He gas mixture in a flow rate of 60 ml/min with temperature ramping at 10 ^{o}C/min until 800 ^{o}C. And the hydrogen consumption was determined using a TCD.

Catalytic activity measurements

The catalytic hydrogenation of *p*-nitrophenol (PNP) was performed at the presence of $NaBH_4$, which can produce active H species trough hydrolysis. In a typical procedure, PNP aqueous solution (150 mL, 500 mg L^{-1}) was mixed with $NaBH_4$ aqueous solution (150 mL, 0.36 M) at the room temperature. After stirring for 5 min, 2mg catalysts were added into the above mixed solution, and the concentration changes of reactants were measured by a UV spectrophotometer at 3 min intervals. Reaction rate was applied to estimate the performance of catalysts, which was calculated as follows:

$$\text{Reaction rate (mol g}^{-1}\text{min}^{-1}) = n_{PNP}\,(\text{mol}) / [m_{catalysts}\,(\text{g}) \times t\,(\text{min})] \quad (1)$$

In which n_{PNP} is the initial mole of PNP, $m_{catalysts}$ is the weight of catalysts and t is the used time PNP conversing completely.

The hydrogenation of 2(5H)-furanone (HFO) with H_2 was carried out in a 100 ml stainless steel autoclave reactor at 80 ^{o}C. 0.4 g of HFO, 2.5 mg catalyst, and 10 ml ethanol were added into the reactor, and the reactor was sealed and flushed with 1 MPa H_2 at least three times to remove the air. Then, the reactor was heated up to 80 ^{o}C in a water bath and introduced with 3 MPa H_2. The reaction was started with continuously stirring. When the reaction was finished, the reactor was cooled down to room temperature in an ice-water bath and then vented H_2 to ambient pressure. The liquid products were analyzed with a gas chromatograph (Shimadzu GC-14C, Rtx-5 capillary column with inner diameter of 0.25 mm and length of 30 m) using a flame ionization detector and identified by gas chromatography/mass spectrometry (GC/MS, Agilent 5890). The GC results were obtained using an internal standard method and n-butanol as standard substrate. The conversion of HFO and selectivity to γ-butyrolactone (GBL) were calculated as follows:

$$\text{Conversion of HFO (\%)} = (n_{F,0}-n_F) / n_{F,0} \times 100 \quad (2)$$

$$\text{Selectivity to GBL (\%)} = n_G / (n_{F,0}-n_F) \times 100 \quad (3)$$

In which $n_{F,0}$ is the initial mole of HFO, and n_F and n_G are the moles of HFO and GBL, respectively.

Electrochemical measurements were conducted on a Zahner potentiostat in a three-electrode configuration, with platinum net as counter electrode and Ag/AgCl as the reference electrode. Amperometry (IT) measured at a constant 0.6 V (vs. Ag/AgCl) in a 0.1 M NaOH electrolyte.

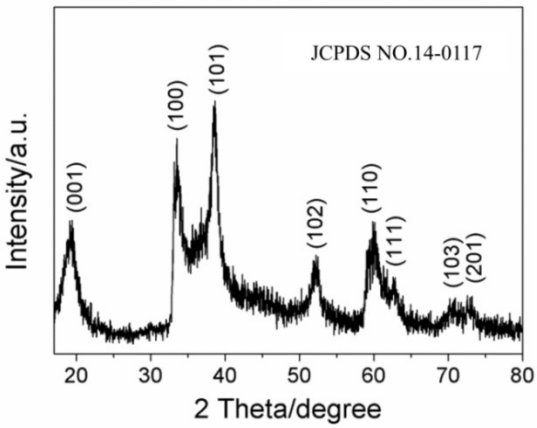

Fig. S1 XRD pattern of $Ni(OH)_2$ precursor.

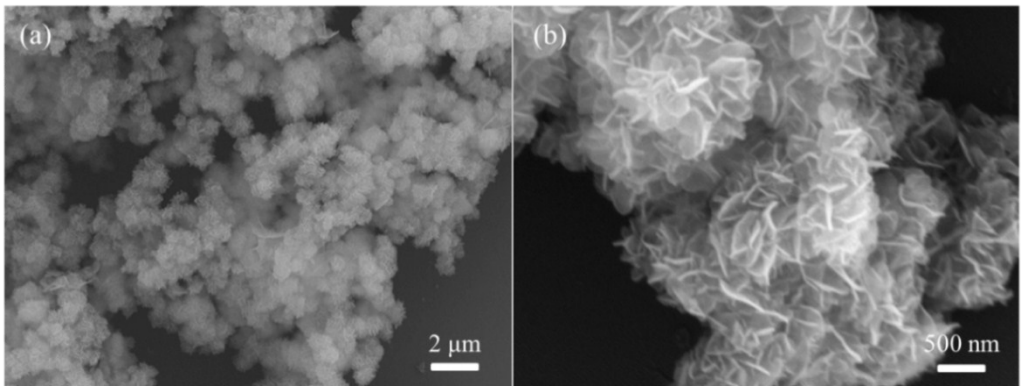

Fig. S2 SEM images of $Ni(OH)_2$ precursor: (a) low magnification, (b) high magnification.

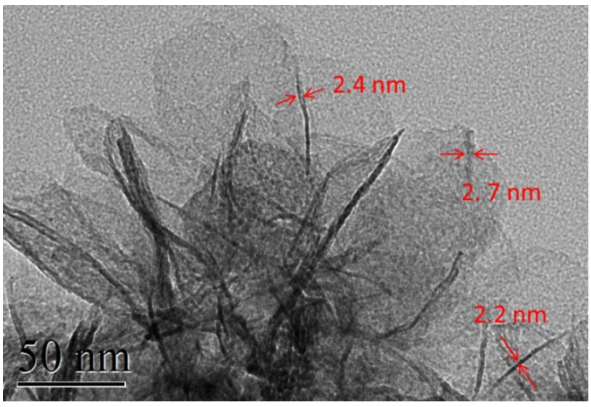

Fig. S3 TEM image of pure NiO.

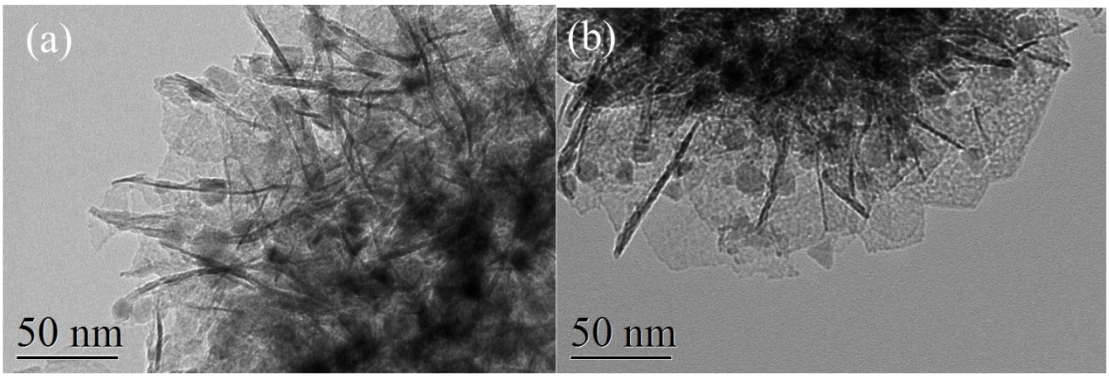

Fig. S4 TEM images of (a) Ni/Ni-450 and (b) Ni/NiO-500.

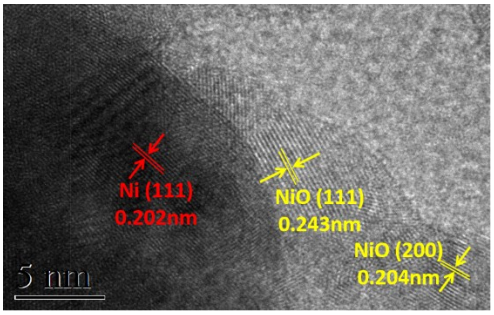

Fig. S5 HRTEM image of the Ni/NiO-500 catalyst.

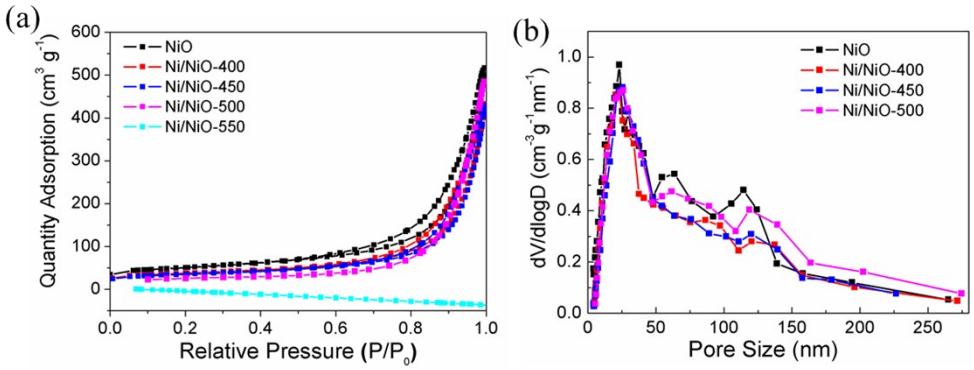

Fig. S6 (a) N_2 adsorption–desorption isotherms and (b) pore sizes distribution for the Ni/NiO composite catalysts obtained at different reduction temperatures.

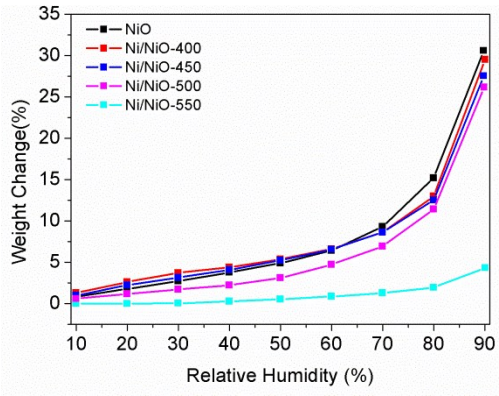

Fig. S7 Water vapor adsorption isotherms of Ni/NiO composite catalysts obtained at different reduction temperatures.

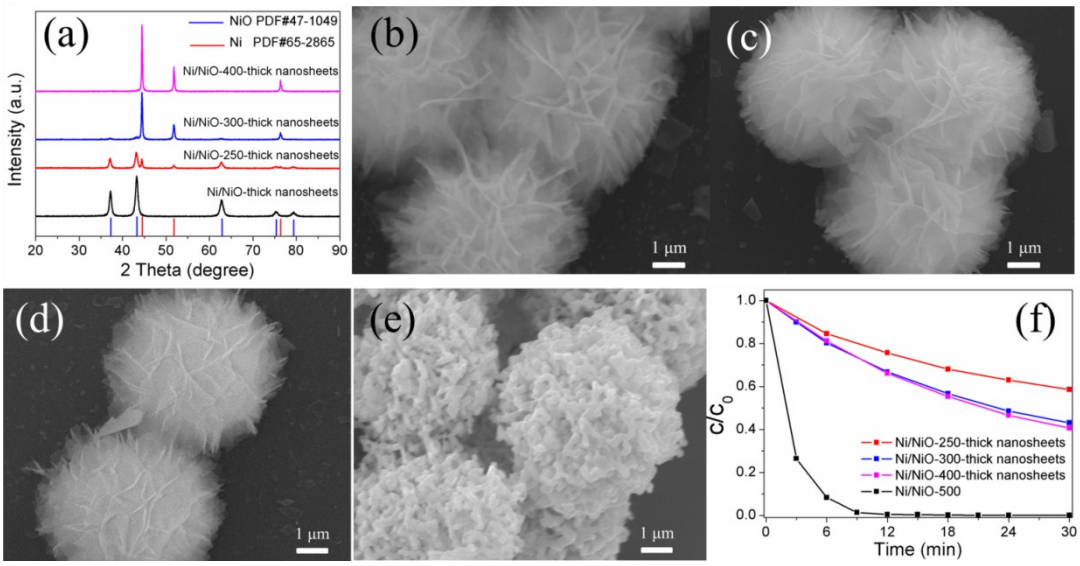

Fig. S8 Characterizations and performance for PNP hydrogenation of Ni/NiO composites with thick nanosheets. (a) XRD patterns of NiO-thick nanosheets reduced at different temperatures; SEM images of (b) Ni/NiO-thick nanosheets, (c) Ni/NiO-250-thick nanosheets, (d) Ni/NiO-300-thick nanosheets and (e) Ni/NiO-400-thick nanosheets; (f) Catalytic hydrogenation efficiency of PNP in different additions versus the reaction time for Ni/NiO composite catalysts with thick nanosheets.

To further verify the unique advantages of the defected ultrathin supports, another Ni/NiO composite catalysts with relatively thick supports were prepared with a similar method, which is shown in Fig. S8**.** It can be seen from Fig. S8(a) that samples reduced at different temperatures are all Ni/NiO composites and their high and sharp diffraction peaks indicate their good crystallinity, which is different from those of samples made up of defected ultrathin nanosheets with relatively broad peaks.

As shown in Fig. S8(b-e), all the samples appear the morphologies of flower-like structures assembly from numerous thick nanosheets with the diameter of about 30 nm, except for the morphology of Ni/NiO-400-thick nanosheets suffers damage because of over-high reduction temperature. The specific surface area and pore structures are listed in Table S1. The specific surface area of NiO-thick nanosheets, Ni/NiO-250-thick nanosheets, Ni/NiO-300-thick nanosheets and Ni/NiO-400-thick nanosheets is 81, 56, 32 and 8 $m^2 \cdot g^{-1}$, which is much smaller than that of samples with ultrathin nanosheets. The mole contents of metallic Ni of Ni/NiO-250-thick nanosheets, Ni/NiO-300-thick nanosheets and Ni/NiO-400-thick nanosheets are calculated to be 34%, 79% and 85%, respectively, according to the EDS results shown in Table S2. The samples were then applied to the hydrogenation of HFO and PNP under the same condition as that in the reaction system of Ni/NiO-500, which is shown in Table 2 and Fig. S8 (f). (The details of Ni/NiO composites with ultrathin nanosheets in the hydrogenation of PNP can be seen in Fig. S10 shown in the followings.) The catalytic efficiency of samples with thick nanosheets are far lower than that of Ni/NiO-500 in both hydrogenation reactions, though the metallic Ni contents of Ni/NiO-300-thick nanosheets and Ni/NiO-400-thick nanosheets are much higher than those of Ni/NiO-500. Therefore, it is again proved that the unique advantages of defect ultrathin nanosheets exhibit in catalysis.

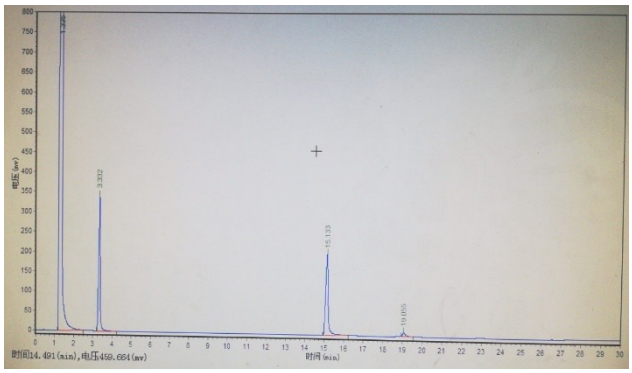

Fig. S9 The typical GC curve for the selective hydrogenation of HFO to GBL.

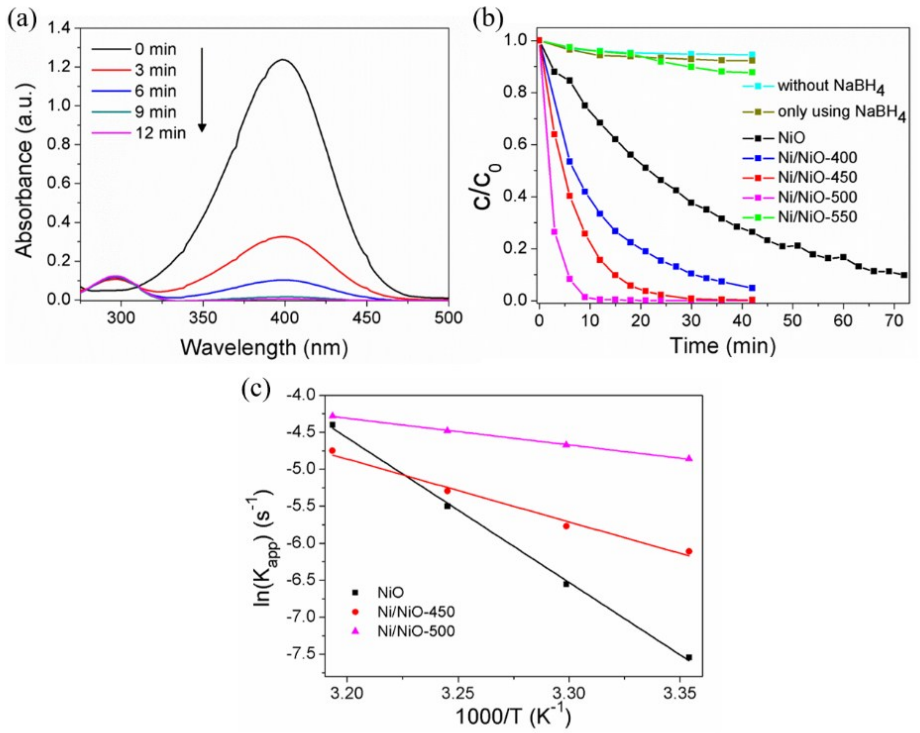

Fig. S10 (a) UV-vis absorption spectra of the hydrogenation of PNP after the addition of samples reduced at 500 °C; (b) Catalytic hydrogenation efficiency of PNP in different additions versus the reaction time. (c) The Arrhenius plot of lnKapp *vs* 1000/T for the catalytic reaction using pure NiO, Ni/NiO-450 and Ni/NiO-500 catalysts, respectively.

Since the superior performance of the Ni/NiO composites has been proven by HFO hydrogenation, it is obvious that such catalysts with unique structures of ultrathin nanosheets and abundant defects also possess substantial potential in various hydrogenation reactions. Therefore, the samples were then applied to the hydrogenation of PNP, which is shown in Fig. S10. In Fig. S10(a), during the catalytic process, the absorption peak at 400 nm decreased sharply, while that at 300 nm increased at the same time, indicating PNP was successfully transformed to *p*-aminophenol (PAP). [3] It is shown in Fig. 8(b) that either catalysts or $NaBH_4$ solution is absent in the system, the concentration of PNP has not clearly changed within 42 min, indicating both of them play important parts in the reduction. Meanwhile, when pure NiO was added into the solution of the presence of both PNP and $NaBH_4$, the conversion of PNP was approximately 70% within 42 min. It was supposed that the hydrogen in the hydrogenation of PNP produced by $NaBH_4$ hydrolysis is highly active

H species, the reaction can be triggered while PNP molecules were adsorbed on NiO ultrathin nanosheets. [4] For Ni/NiO-400, the conversion increased to 90% within 42 min, which is attributed to the presence of Ni nanoparticles that can dissociate and activate the hydrogen more effectively as well as facilitate the electron transfer in the reaction process. Furthermore, for Ni/NiO-450 and Ni/NiO-500, the Ni amounts continued to increase and the conversion upgraded to 100% within 30 min and 12 min, respectively. However, Ni/NiO-550, whose morphology had been completely destroyed and whose specific surface area was close to zero, exhibited ultralow catalytic activity, with just approximately 10% conversion in 42 min. Moreover, the apparent activation energy (Ea) was calculated to be 162.1, 70.5 and 29.8 kJ/mol for pure NiO, Ni/NiO-450 and Ni/NiO-500, respectively, according to Arrhenius equation, as shown in Fig. S10(c). Obviously, the appearance of metallic Ni can largely decrease the value of Ea and make the reaction more easily to be triggered. Based on the analysis mentioned above, Ni/NiO-500 with the most metal active sites as well as a unique support structure with ultrathin nanosheets and abundant defects exhibited ultrahigh activity in the hydrogenation of PNP at room temperature, which is even superior to most reported noble metals, as shown in Table S3.

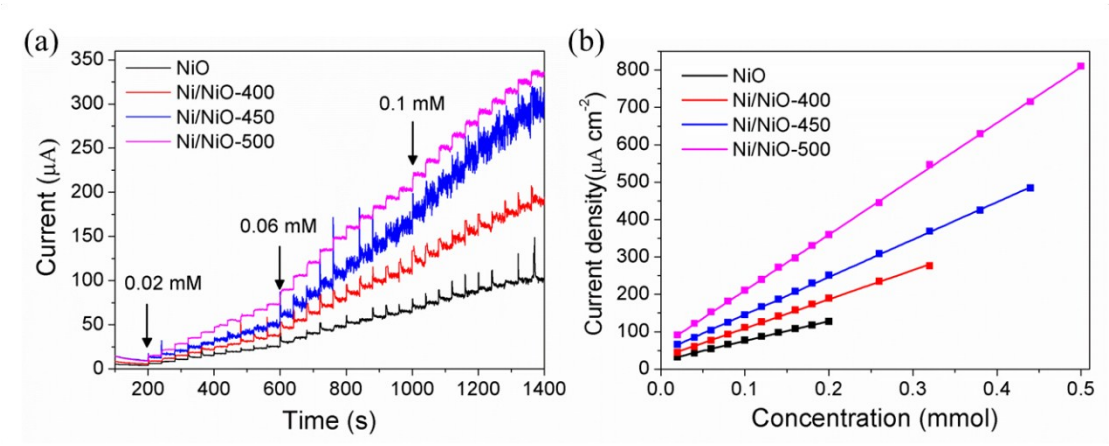

Figure. S11 (a) Amperometric response of Ni/NiO composite electrodes with successive addition of glucose at 0.6 V; (b) The linear dependence of steady current of Ni/NiO composite electrodes on concentration of glucose.

In addition, such catalysts with unique mesostructures were also considered to possess excellent electrocatalytic properties, and they were further applied to nonenzymatic glucose sensing. As shown in Figs. S11(a-b) and Table S4, for Ni/NiO-500, the linear detection range can be as large as 20-500 μM and the sensitivity can be up to approximately 1,494.2 $\mu A \cdot mM^{-1} \cdot cm^{-2}$. At the same time, the detection limit was estimated to be approximately 5.1 μM (signal-to-noise ratio of 3). Compared with most reported results, it displays a broader linear range, a higher sensitivity and a lower detection limit, which is shown in Table S5.

Table S1. Specific surface area and pore structures of the Ni/NiO composite catalysts with thick nanosheets.

Sample	Specific surface area ($m^2 g^{-1}$)	Pore size (nm)	Pore volume ($cm^3 g^{-1}$)
NiO-thick nanosheets	81.87	4.56	0.08
Ni/NiO-250-thick nanosheets	56.51	9.07	0.07
Ni/NiO-300-thick nanosheets	32.12	17.76	0.03
Ni/NiO-400-thick nanosheets	8.76	21.38	0.01

Table S2. EDS results for the Ni/NiO composite catalysts with thick nanosheets.

Sample	Ni atomic%	O atomic%	Metallic Ni mole%
Ni/NiO-250-thick nanosheets	60.23	39.77	34
Ni/NiO-300-thick nanosheets	83.07	16.93	79
Ni/NiO-400-thick nanosheets	86.34	13.66	85

Table S3 Comparison of the catalytic hydrogenation of PNP among Ni/NiO-500 and other catalysts.

Catalysts	PNP concentration ($\times 10^{-3}$ mmol)	Catalyst amount (mg)	Time (min)	Conversion (%)	Reaction rate ($\times 10^{-3}$ mol · min^{-1} · g^{-1})	Ref.
Ni/NiO-500	540	2	12	100	22.50	this work
Ni/C	540	2	42	29	1.86	this work
Ni	25	1	18	70	0.97	5
$Ni_{0.22}$/carbon black	25	1	9	100	2.78	5
Ni@Graphene	10	1	12	100	0.83	6
AuPt@Au NCs/rGO	0.35	0.05	6	100	1.17	7
Au-CeO_2	0.15	0.07	4	100	0.54	8
PdNiP/RGO	10	3	3	100	1.11	9
Co/Al_2O_3	0.2	0.2	4	100	0.27	10
Co@NC	0.125	0.02	3	100	2.08	11
Cu/Cu_2O@C-rGO	0.5	0.1	1.5	100	3.33	12
Co_xFe_{1-x}@N-G	10	2	3	100	1.67	13
Pt/Fe_2O_3	0.25	5	12	100	0.0042	14
Cu/CuO-Ag	0.5	1.5	1.25	100	0.27	15
Pd/Au@g-C_3N_4-N	14.38	0.25	3.5	95	15.61	16

Table S4. Performance of electrochemical sensing for glucose of Ni/NiO catalysts.

Sample	Linear range (μM)	Sensitivity (μA·mM^{-1}·cm^{-2})	Detection limit (μM)
NiO	20 ~200	532.6	14.2
Ni/NiO-400	20 ~320	779.5	9.8

Ni/NiO-450	20 ~440	1003.5	8.1
Ni/NiO-500	20 ~500	1494.2	5.1

Table S5. Comparison of the electrochemical sensing for glucose among Ni/NiO-500 and other catalysts.

Sample	Linear range (μM)	Sensitivity ($\mu A \cdot mM^{-1} \cdot cm^{-2}$)	Detection limit (μM)	Reference
Ni/NiO-500	20 ~500	1494.2	5.1	this work
PINA(SDS)/$Ni(OH)_2$ modified CPE	160~750	584	90	17
NiO/Ni foam	18~1200	395	6.15	18
CoOOH nanosheet arrays	up to500	967	10.9	19
Pt nanoflowers	1000~16000	1.87	48	20

Reference

1. F, Cao, F. Zhang, R. P. Deng, W. Hu, D. P. Liu, S. Y. Song and H. J. Zhang, *CrystEngComm*, 2011, **13**, 4903.
2. P. J. Liu, V. M. H. Ng, Z. J. Yao, J. T. Zhou, Y. M. Lei, Z. H. Yang, H. L. Lv and L. B. Kong, *ACS Appl. Mater. Interfaces,* 2017, **9**, 16404.
3. X. Wang, R. Y. Cao, S. W. Zhang, P. Y. Hou, R. X. Han, M. H. Shao and X. J. Xu, *J. Mater. Chem. A,* 2017, **5**, 23999.
4. D. D. Jia, H. Y. Gao, W. J. Dong, S. Fan, R. Dang and G. Wang, *ACS Appl. Mater. Interfaces,* 2017, **9**, 20476.
5. J. W. Xia, G. Y. He, L. L. Zhang, X. Q. Sun and X. Wang, *Appl. Catal. B: Environ.,* 2016, **180**, 408.

6. J. W. Wu, W. Liu, X. Xiang, K. Sun, F. H. Liu, C. Cai, S. B. Han, Y. Y. Xie, S. A. Li and X. T. Zu, *Carbon*, 2017, **117**, 192.
7. Q. Liu, Y. R. Xu, A. J. Wang and J. J. Feng, *RSC Adv.,* 2015, **5**, 96028.
8. C. M. Fan, L. F. Zhang, S. S. Wang, D. H. Wang, L. Q. Lu and A. W. Xu, *Nanoscale*, 2012, **4**, 6835.
9. X. Gao, H. Zhao, Y. G. Liu, Z. P. Ren, C.P. Lin, J. L. Tao and Y. P. Zhai, *Mater. Chem. Phys.,* 2019, **222**, 391.
10. X. Wang, R. Y. Cao, P. Y. Hou, R. X. Han, M. H. Shao and X. J. Xu, *J. Mater. Chem. A,* 2017, **5**, 23999.
11. X. Y. Li, C. M. Zeng, J. Jiang and L. H. Ai, *J. Mater. Chem. A.,* 2016, **4**, 7476.
12. K. Yang, Y. Yan, H. Y. Wang, Z. X. Sun, W. Chen, H. T. Kang, Y. Han, W. Q. Zhang, X. H. Sun and Z. X. Li, *Nanoscale,* 2018, **10**, 17647.
13. B. K. Barman and K. K. Nanda, *ACS Sustainable Chem. Eng.,* 2018, **6**, 12736.
14. P. Zhang, X. Y. Yang, H. L. Peng, D. Liu, J. F. Wei and J. Z. Gui, *Catal. Commun.,* 2017, **100**, 214.
15. Y. Liang, Z. Chen, W. Yao, P. Y. Wang, S. J. Yu and X. K. Wang, *Langmuir,* 2017, **33**, 7606.
16. W. Fang, Y. C. Deng, L. Tang, G. M. Zeng, Y. Y. Zhou, X. Xie, J. J. Wang, Y. Wang and J. J. Wang, *J. Colloid Interf. Sci.,* 2017, **490**, 834.
17. R. Ojani, J. B. Raoof and B. Norouzi, *J. Solid State Electrochem*, 2011, **15**, 1139.
18. L. Wang, Y. Z. Xie, C. T. Wei, X. P. Lu, X. Li and Y. H. Song, *Electrochim. Acta,* 2015, **174**, 846.
19. K. K. Lee, P. Y. Loh, C. H. Sow and W. S. Chim, *Electrochem. Comm*., 2012, **20**, 128.
20. M. Q. Guo, H. S. Hong, X. N. Tang, H. D. Fang and X. H. Xu, *Electrochim. Acta*, 2012, **63**, 1.